Ion-induced nanopattern propagation on metallic surfaces

Tomáš Škereň,[1,*] Martin Veselý,[2] Pavel Čapek,[2] and Jaroslav Král[1]

[1]*Czech Technical University in Prague, Faculty of Nuclear Sciences and Physical Engineering, Břehová 7, 115 19 Prague 1, Czech Republic*

[2]*University of Chemistry and Technology, Faculty of Chemical Technology, Technická 5, 166 28 Prague 6, Czech Republic*

(Received 30 January 2015; revised manuscript received 5 October 2015; published 3 December 2015)

We investigate the formation of ion-induced patterns on single-crystalline Ni(001) bombarded with a 20-keV Ga^+ ion beam. For near normal ion incidence isotropic roughness forms on the surface. By moving to grazing incidence this pattern gradually transforms into a pronounced ripple pattern with wave vector perpendicular to the ion beam. By using an *in situ* scanning electron microscope we were able to analyze the real-time dynamics of the pattern formation process and evaluate the direction and velocity of the net in-plane morphology propagation for different angles of ion incidence. We compare the experimental results to the predictions of the classical theory for the pattern formation.

DOI: 10.1103/PhysRevB.92.235406 PACS number(s): 81.65.Cf, 79.20.Rf, 64.75.Yz

I. INTRODUCTION

Irradiation of surfaces with low-energy ion beams can lead to the formation of self-organized periodic surface morphology at nanoscale in the form of ripples [1–5], mounds/pits [6–11], or even more intricate patterns [12–15]. This phenomenon has attracted a lot of attention due to its potential as an efficient tool for modification of physical properties of surfaces [16–22]. However, the general understanding of the phenomenon remains incomplete and a number of questions remain open [23–26].

An interesting aspect of the pattern formation dynamics is the in-plane propagation of the pattern during oblique angle ion bombardment. This behavior was initially predicted by Bradley and Harper [27]. By extending the Sigmund approach to the description of the sputtering process [28] they derived the well-known Bradley-Harper instability [27]. The in-plane pattern propagation emerged from the derivation as a side-effect—by oblique ion incidence the pattern was predicted to travel in the direction parallel to the ion-beam projection to the sample surface. The velocity, and even direction, varies with the angle of ion incidence and is determined by the sputter yield angular dependence as [27,29,30]

$$v = -\phi\Omega\left(\cos\theta\frac{dY(\theta)}{d\theta} - Y(\theta)\sin\theta\right), \tag{1}$$

where ϕ is the ion flux, Ω is the volume occupied by one atom in the target material, θ is the angle of ion incidence (measured from the surface normal), and $Y(\theta)$ is the sputter yield. However, the experimental investigation of this aspect of the pattern formation is technically challenging and was not performed until late 1990s.

The usual experimental approach to the investigation of the ion-induced pattern formation is to, first, perform the ion irradiation and subsequently observe the resulting surface morphology *ex situ*. The pattern evolution is visualized by preparing multiple samples using different ion fluences and observing the pattern in different stages of the evolution. This approach does not allow for direct visualization of the pattern propagation.

Various techniques were used to study the pattern evolution *in situ* and in real-time—x-ray scattering [8,9,31–35], light scattering spectroscopy [36–40], high-resolution low-energy electron diffraction [41,42], and even He atom scattering [43,44]. However, neither of these techniques is capable of resolving the in-plane pattern propagation.

The direct microscopic observation of the pattern formation dynamics and, in particular, of the pattern propagation was only performed by the use of instruments combining the focused ion beam (FIB) with scanning electron microscopy (SEM) [30,45–48] (a number of studies used FIB as well but did not focus on the pattern propagation [49–51]). A slightly different approach was used in [29] where, although a FIB instrument was used as well, *ex situ* ion irradiation with Xe ions was performed in order to exclude a possible influence of Ga implantation in Si. These experimental observations of the pattern propagation attracted a lot of attention since in some cases the observed behavior was in direct contradiction to the theoretical predictions [45] which greatly helped to improve the physical understanding of the phenomenon [52].

It is well known that the ion-induced pattern formation shows complicated behavior with respect to the target material. Perhaps the clearest contrast can be seen between the behavior of amorphizable and metallic surfaces. While the majority of the studies focusing on semiconductors and dielectric materials investigate the so-called parallel mode ripples (PaMR—the orientation of the pattern wave vector is parallel to the ion-beam projection) the metallic surfaces usually exhibit only the perpendicular mode ripple formation (PeMR) [3,18,53,54]. All the studies that investigated the pattern propagation so far focused on the propagation of PaMR ripples on amorphous (amorphized) surfaces. Several studies investigated the pattern formation on metallic surfaces by focused ion beam [55,56] but, so far, no investigation of the ripple pattern propagation on metals exists.

In this paper we investigate the formation of ion-induced patterns on a Ni (001) surface irradiated with a focused Ga^+ ion beam. We study in detail the evolution and propagation of the surface morphology during the pattern formation process. We compare the measured pattern velocity with the predictions of the sputtering theory and we discuss the results.

*t.skeren@gmail.com

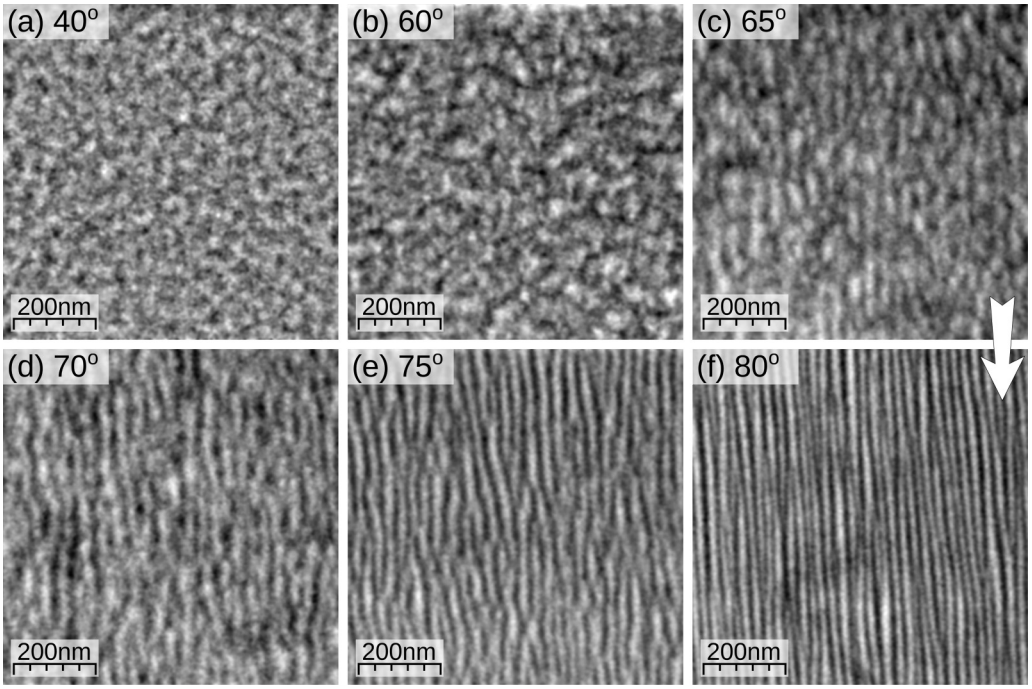

FIG. 1. SEM micrographs of the Ni(001) surface after Ga ion irradiation at different angles of incidence. The ion fluence is about 320 ions nm^{-2}; the arrow indicates the azimuthal direction of the ion beam.

II. EXPERIMENTAL

One-hundred-nanometer-thick epitaxial Ni(001) thin films were grown by molecular-beam epitaxy on MgO substrates. Prior to the growth, the substrates were annealed to 600°C for 30 min and subsequently cooled to the growth temperature of 180°C. Ni was evaporated by an electron gun with a deposition rate of 0.1 nm s^{-1}. The base pressure of the chamber was below 10^{-9} mbar. After the growth, the samples were annealed to 700°C for 1 h. A thin gold capping layer (3 nm) was subsequently deposited on the annealed films at room temperature to prevent oxidation. This initial roughness induced by the gold cap may slightly speed up the onset of the pattern formation but is not expected to affect the patterning process in the later stages [53,57]. Finally, the samples were taken out of the vacuum and kept in ambient conditions.

Focused ion-beam (FIB) experiments were performed at the University of Chemistry and Technology using the Tescan LYRA3 dual beam instrument. *Ex situ* samples were inserted in the SEM vacuum chamber where the base pressure was about 2×10^{-6} mbar. All the experiments were performed at room temperature. The typical FIB current during the ion irradiation was ∼100 pA. The beam, which was slightly defocused in order to avoid inhomogeneities in the ion fluence, was rastering over an area of $10 \times 10\ \mu$m with a frequency of about 20 Hz. For off-normal ion irradiation the azimuthal direction of the ion beam was parallel (within a few degrees) to the (100) plane of the Ni film.

For each angle of incidence the irradiation sequence consisted of more than ten equivalent sputtering steps between which an SEM image of the surface was taken. The sequence was finished when all the Ni film was sputtered away—this was clearly observable by sudden change in the SEM contrast. This approach gave us good knowledge of the absolute thickness of the sputtered material during the irradiation sequence. We estimated the possible error, caused mainly by the presence of surface roughness and ion intermixing, to about 5%.

The Ga content in the Ni sample surface was investigated *in situ* by the energy-dispersive x-ray spectroscopy (EDS) using the same dual beam instrument.

III. RESULTS

A. Angular dependence

The majority of the previous studies of ion-induced pattern formation on metallic surfaces were performed with noble gas ions. In this study we used a 20-keV Ga^+ ion beam of the FIB instrument to sputter the Ni(001) surface. The surface morphology after ion irradiation at different angles of incidence and fluence of about 320 ions nm^{-2} is presented in Fig. 1. It generally follows the same qualitative trend as previously observed on other metallic surfaces—isotropic roughness formation at low angles of incidence and gradual transition towards a well-defined PeMR pattern at grazing incidence [53]. The pattern wavelength and correlation length [53] for the surfaces from Fig. 1 are presented in Fig. 2.

B. Ga content

In contrast to noble gas ions the presence of Ga in the sample surface can substantially influence the process of pattern formation, most notably by precipitation of additional phases. The influence of Ga on the ion-induced pattern formation on Si has been investigated by [29]. In general, the incorporation of Ga in semiconductors represents a substantial issue since it is expected to segregate from the matrix material and form buried nanoclusters [29].

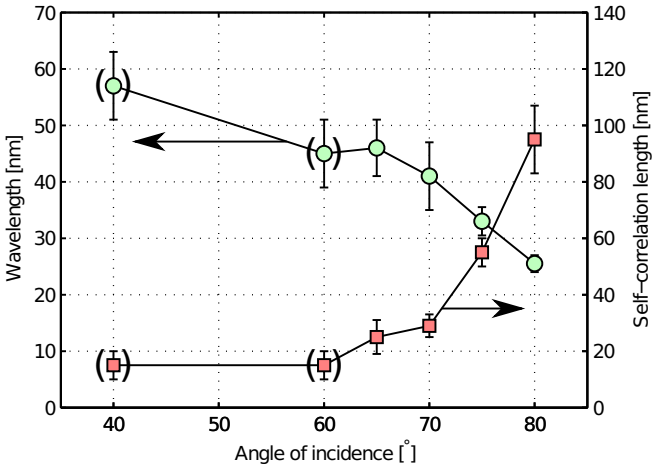

FIG. 2. (Color online) Wavelength and self-correlation length of the ion-induced pattern on the Ni(001) surface bombarded by about 320 ions nm^{-2} fluence of Ga ions as a function of the angle of incidence. Parentheses indicate that no prominent ripple pattern is formed.

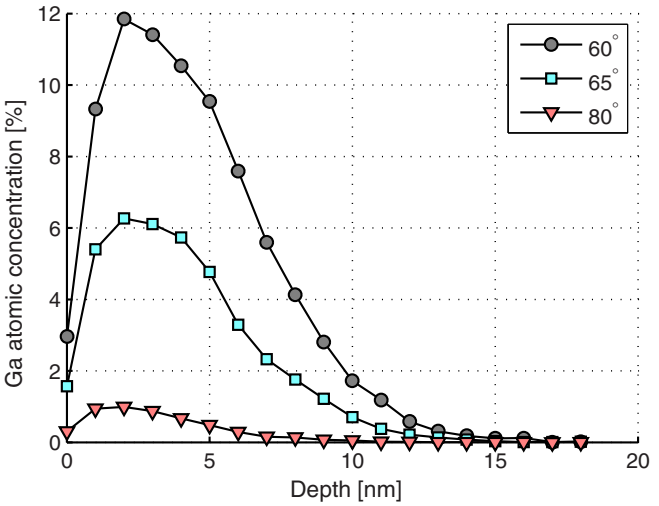

FIG. 3. (Color online) Estimated depth profile of the Ga concentration in the eroded Ni surface.

In the case of metallic surfaces the Ga at sufficiently low concentrations is expected to mix with the matrix. The possible influence of the Ga incorporation on the pattern formation on the Cu surface was previously discussed in [56], where scanning transmission electron microscopy confirmed that up to 20% of Ga was present in the Cu surface. However, the Ga did not contribute to any additional phase formation and was distributed homogeneously underneath the surface. The authors concluded that the Ga is unlikely to influence the qualitative behavior of the ion-induced pattern.

In order to evaluate the possible role of Ga in the present system we performed EDS measurements to estimate the Ga content in our samples. The solubility of Ga is expected to be around 10% at room temperature [58]. First, we measured the time required to sputter the whole 100-nm-thick Ni film away. We then sputtered the film for half the total time, making sure that we were left with a 50-nm-thick Ni film. We assumed that at this point the Ga content in the surface had already reached the saturation level. We measured the EDS spectrum and by comparing the Ni and Ga signal we were able to estimate the total amount of Ga present in the surface. Finally, we performed Monte Carlo simulations using SRIM software package [59,60] to calculate the Ga implantation profile and to estimate the depth profile of the atomic concentration of the Ga. We repeated the procedure for three different angles of ion incidence and the results are presented in Fig. 3. In this estimation we used a static Ga implantation profile, i.e., sputtering was not taken into account. Because of the sputtering, the real profile is slightly shallower and the absolute Ga concentration is slightly higher.

The EDS measurements show that for 60° angle of incidence the Ga concentration may reach the solubility limit and the presence of additional phases cannot be fully excluded. However, for 65° angle of incidence and above the Ga concentration seems to be already well below the solubility limit and the surface material should be homogeneous.

C. Pattern propagation measurement

In order to observe the propagation of the ion-induced morphology we performed *in situ* SEM observation of the FIB irradiated Ni surface. Prior to the nanopattern formation we milled two linear trenches in the surface to serve as a mark for precise alignment of the subsequent SEM micrographs. The trenches were 10 μm long, 0.5 μm wide, several μm deep, and 2 μm apart. Figure 4 shows an SEM micrograph of these trenches along with the optical microscope images and the relative position of the sputter craters with respect to the trenches.

In the next stage, a sequence of irradiation steps was performed and an SEM image was taken after each step. The approximate location of the SEM imaging area is outlined by the square in Fig. 4(c)—this area always covered both the tails of the trenches and a portion of unaffected patterned surface. Subsequently, the images were aligned according to the trench position and cropped. The trenches were sufficiently deep so that their bottom was not reached by the obliquely incident ion beam and the rough morphology present there was ideal to precisely align the frames of the sequence. An example of three aligned and cropped consecutive frames from an irradiation sequence at 75° angle of incidence is presented in Fig. 5. This procedure was repeated for five different angles of incidence.

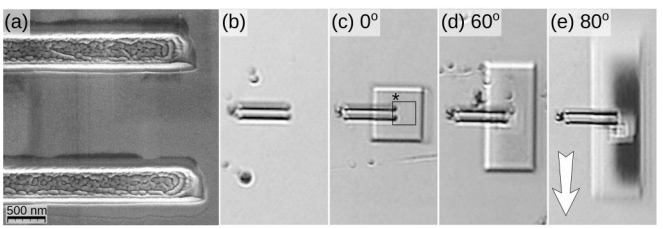

FIG. 4. (a) SEM and (b) optical microscope image of the alignment marks for the pattern propagation measurement. (c–e) Optical microscope images of the sputter craters after irradiation at different angle of incidence with the alignment marks visible; the arrow indicates the azimuthal direction of the ion beam.

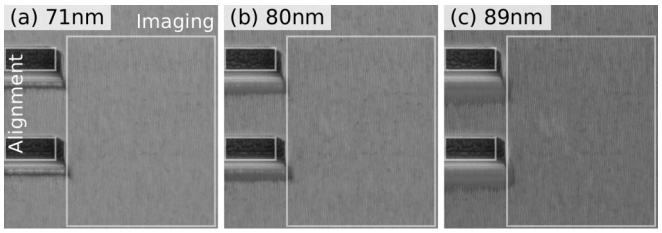

FIG. 5. Three aligned consecutive micrographs from the sputtering sequence at 75° angle of incidence. Crater depth is indicated in the panel header; alignment and imaging areas are highlighted.

IV. DISCUSSION

In the following we first discuss the general aspects of the propagation of the PeMR pattern. Further we present a procedure we used to extract the pattern propagation velocity and we discuss its meaning and reliability. Finally we compare the experimental data for the propagation velocity with the prediction of the theoretical model.

A. Feature propagation in the PeMR pattern

The very definition of the morphology propagation phenomenon is not trivial. In the most simple case, when the surface has a corrugated morphology which does not evolve with time but only travels in the surface plane, we can define the propagation velocity easily. However, if the morphology changes during the ion irradiation, in order to observe the propagation, we need to be able to link specific morphological features in the surface pattern and measure their motion. This is only possible if the surface evolution is sufficiently slow and specific features persist on the surfaces for a sufficient amount of time to observe their collective propagation.

In the case of propagation of the PaMR pattern, the propagation direction is perpendicular to the ripple orientation and we can simply follow the travel of the ripple crests. However, in the case of PeMRs, the propagation direction is parallel to the ripple orientation and the morphology propagation is only visible thanks to defects and imperfections in the ripple pattern. In other words, a perfect PeMR pattern cannot propagate.

Figure 6 shows sections of three subsequent frames of a sputtering sequence at 75° angle of incidence and the lower row shows the same images with ripple crests highlighted. We can see that the ripple morphology in the three frames is not identical: some ripples seem to elongate, while others change their shape, or even vanish; however, we can visually identify certain features in the morphology which seem to persist. In the course of these three frames, these features seem to travel downwards (white lines join these seemingly corresponding features in the lower row of Fig. 6). By investigating a large number of such features, we could estimate the propagation velocity.

However, this approach is obviously very tedious and, more importantly, subjective. In the following we discuss an alternative way of measuring the pattern propagation.

B. Pattern cross correlation

A more robust and systematic approach to investigate the pattern propagation is by looking for the cross correlation between subsequent frames of the sputtering sequence. The cross correlation $\star$ of two real functions $f(x,y)$ and $g(x,y)$ is defined as

$$(f \star g)(u,v) = \int f(x,y)g(x+u,y+v) \qquad (2)$$

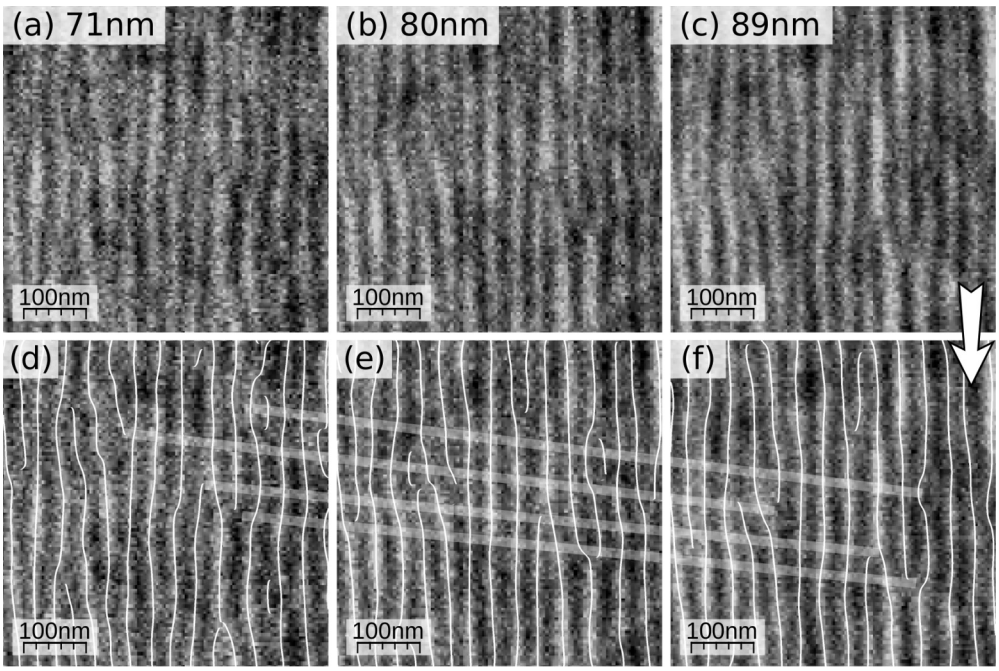

FIG. 6. (a–c) 500 × 500-nm SEM micrographs of corresponding areas on three consecutive frames of the sputtering sequence at 75° angle of incidence (crater depths indicated in the panel headers). (d–f) The same micrographs with ripple crests highlighted. The thicker white lines connect seemingly corresponding features in the ripple pattern; the white arrow indicates the ion-beam azimuthal direction.

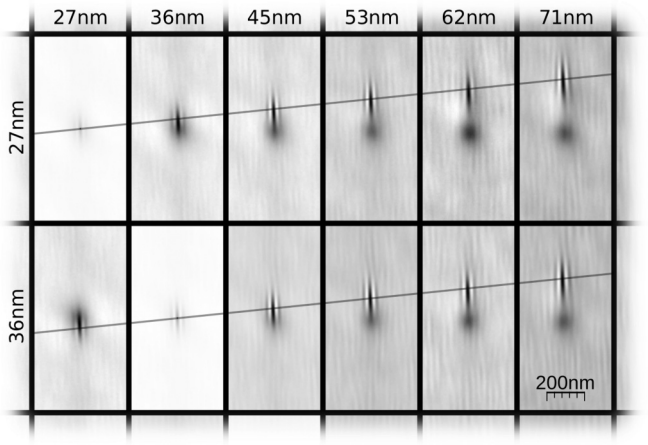

FIG. 7. Cross-correlation functions of some of the frames from the sputtering sequence at 75° angle of incidence; sputtered depth for rows and columns indicated in the top and left, respectively. Each tile represents a central part of the respective correlation function with dimensions 500 × 1000 nm^2. The inclined line approximately indicates the travel of the correlation maximum for increasingly distant frames of the sequence.

and can be also evaluated using Fourier transform

$$(f \star g) = \mathcal{F}^{-1}[\mathcal{F}(f)^* \mathcal{F}(g)] \tag{3}$$

where $\mathcal{F}$ stands for the Fourier transform and * is a complex conjugate. If functions f and g are defined on a finite and discrete support (such as the SEM image data), we can replace the Fourier transform in Eq. (3) by its discrete counterpart and use a formally identical formula to evaluate the cross correlation between the two images. By using the discrete Fourier transform we inherently perform periodization of the images. This does not affect the result if the image area is substantially larger than the area where the correlation function is nonzero (this condition was well fulfilled in the processing of our SEM data).

The cross-correlation function essentially reflects the "similarity" between the two functions f and g. If the cross-correlation function of f and g has a maximum, we say that f and g are correlated. If $f = g$ the cross correlation (called self-correlation in this case) has a maximum at (0,0). If $f(x,y)$=$g(x-u, y-v)$, i.e., g is identical to f but shifted by (u,v), the cross-correlation function has a maximum at (u,v). As such, the cross correlation is an ideal tool to investigate the pattern propagation—the presence of a pronounced correlation maximum indicates that there is a similarity between the morphologies and its eventual offset from the center indicates relative shift between the corresponding features.

For a sequence of frames f_i we can calculate the cross correlations $h_{i,j} = f_i \star f_j$. Figure 7 shows some of these correlation functions for the sputtering sequence at 75° angle of incidence arranged in a matrix—the i,jth tiles in the matrix represent $h_{i,j}$. The diagonal of this matrix, obviously, shows the self-correlation functions of the frames. Distance 1 from the diagonal means cross correlation of two consecutive frames; if we go further from the diagonal, we are looking at cross correlation of more distant frames in the sequence. The matrix is symmetric by its diagonal, except for the fact that the corresponding tiles are inverted by their center (a result of the frames coming into the correlation calculation in reversed order).

As we can see in Fig. 7, there are pronounced maxima in the cross-correlation functions. Interestingly, these maxima are present not only for the subsequent frames (distance 1 from the diagonal) but even for more distant frames of the sequence. The very presence of these maxima indicates that the surface morphology retains some of its features, i.e., remains self-similar, even after prolonged ion irradiation. Obviously, the pattern also undergoes evolution, for instance the pattern wavelength changes during the process, but the existence of the maximum indicates that there is some remaining similarity.

The offset of these maxima from the center indicates that the "similar" features in the two frames are shifted with respect to each other. We can see that this offset increases linearly with the distance from the matrix diagonal, i.e., the offset of the maximum between two frames is proportional to their distance in the sputtering sequence. This observation consistently indicates that the pattern is propagating during the irradiation sequence and we can readily evaluate the propagation velocity by measuring the offset of the correlation maximum between consecutive frames.

The outlined procedure is, in fact, a very suitable candidate for the very definition of the pattern propagation—if there is a nonzero correlation between consecutive frames of the sequence we can say that the morphology remains self-similar and the offset of the correlation maximum then indicates the amount of the in-plane travel between the two frames.

Additionally, careful inspection of the cross-correlation functions in Fig. 7 also reveals the presence of central maxima (blurred dark spots in the middle of the tiles). These maxima indicate that there is a component in the measured SEM images that persists between frames but, in contrast to the discussed PeMR morphology, remains static. Such features are visible even directly in the SEM micrographs as large darker and brighter areas. These features are likely caused by the Ni film structure which, even though it is epitaxial, has a granular structure with a few-degree out-of-plane texture. This crystalline orientation variation probably creates a contrast during the SEM imaging which clearly remains static during the ion irradiation, since the grains have a fixed position in the film. The presence of this central correlation maximum does not impose a direct problem for the pattern propagation measurement. However, in the case of nearby frames (distance 1 from the diagonal of the correlation matrix) the central spot may interfere with the correlation maximum of the PeMR morphology and precise localization of its position may be difficult.

In order to facilitate this procedure and, particularly, if we want to evaluate the pattern propagation automatically, it is useful to perform spectral filtering of the SEM images. Figure 8(a) shows a section of a frame from the sputtering sequence and Fig. 8(b) shows a Fourier spectrum of this frame. The central peak in the spectrum corresponds to the larger static features in the topographs, while the satellite maxima represent the ripple morphology. By performing a bandpass filter which only lets the satellite maxima pass we can suppress the noise, enhance the ripple morphology, and get rid of the artifacts mentioned in the previous paragraph [Fig. 8(c) shows the image from Fig. 8(a) after bandpass filtering while

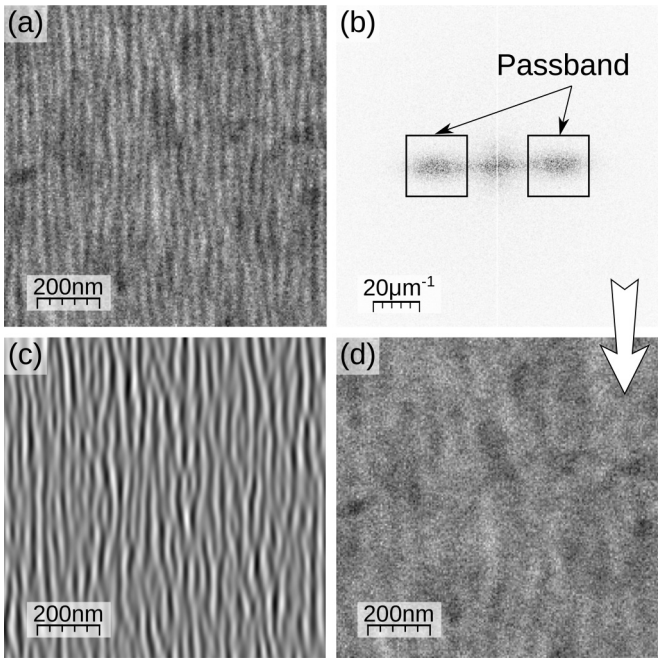

FIG. 8. (a) Part of an SEM image from a sputtering sequence at 75° angle of incidence. (b) Fourier spectrum of the same frame with the passband of the filter indicated. (c) Image from panel (a) after bandpass filtering. (d) Morphology from panel (a) suppressed by the bandpass filter.

Fig. 8(d) shows the residual morphology, that was suppressed by the filtering]. This procedure was also used to identify and highlight the ripple crests in Figs. 6(d)–6(f).

After the filtering, we can again calculate the cross correlations between the frames and arrange them in a matrix (Fig. 9). The central maxima are now suppressed and the evaluation of the peak position is now easier and more precise.

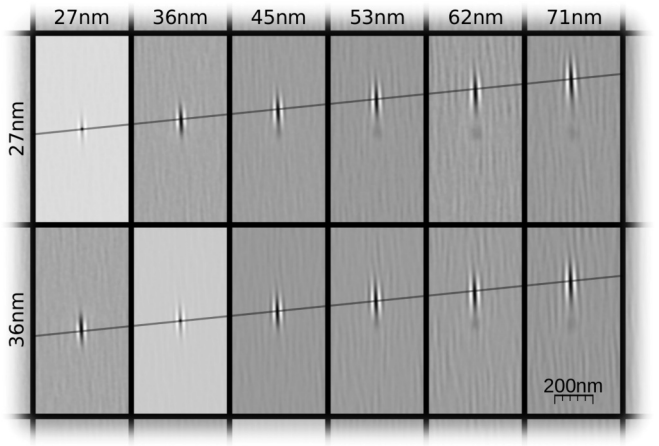

FIG. 9. Cross-correlation functions of some of the frames from the sputtering sequence at 75° angle of incidence after spectral filtering; sputtered depth for rows and columns indicated in the top and left, respectively. Each tile represents a central part of the respective correlation function with dimensions 500 × 1000 nm^2. The inclined line approximately indicates the travel of the correlation maximum for increasingly distant frames of the sequence.

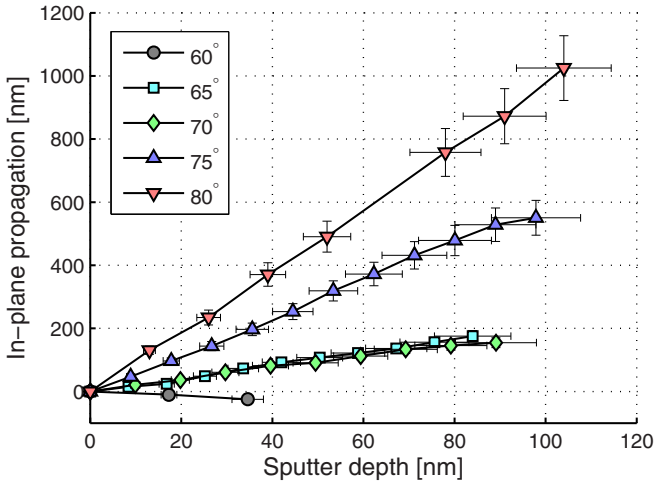

FIG. 10. (Color online) In-plane propagation of the surface morphology as a function of sputtered depth for different angles of ion incidence. Positive velocity indicates propagation away from the ion source.

We evaluated the pattern propagation for all the measured sputtering sequences, and the pattern travel as a function of the sputtered depth is presented in Fig. 10 for different angles of ion incidence. There are several experimental uncertainties that contribute to the total error of this procedure. First, we include a 10% error on the sputter depth due to the uncertainty in the estimation of the moment when the whole Ni film was sputtered away. The error of the propagation distance measurement can be estimated by looking at the transverse (x axis) position of the cross-correlation peaks in Fig. 7. Ideally, there is no physical reason that these peaks would travel in the direction perpendicular to the ion-beam projection but in reality there is some scatter in their precise x position. This scatter is caused by a combination of alignment imperfections, nonlinear distortion of the SEM images, ion-beam direction, and SEM scanning direction misalignment. Finally, it is reasonable to expect that a similar error influences also the measurement of the peak position in the propagation direction and this is how we obtained the vertical error bars in Fig. 10.

C. Comparison to the theoretical model

In order to compare the experimentally measured values of the pattern propagation velocity with theoretical predictions of the sputtering theory we define the relative propagation velocity v_r as a ratio of the lateral propagation velocity v and vertical erosion velocity $v_e = \phi\Omega Y(\theta)\cos\theta$:

$$v_r = -\frac{1}{Y(\theta)}\frac{dY(\theta)}{d\theta} + \tan\theta, \qquad (4)$$

which can be intuitively described like this: if 1 nm of material is sputtered away the pattern moves v_r nanometers in plane in the direction away from the ion source. The measured relative propagation velocity for different angles of incidence is presented in Fig. 11.

The sputter yield angular dependence was approximated by the Yamamura formula [61]:

$$Y(\theta) = Y_0 \cos^{-f}\theta \exp[f(1-\cos^{-1}\theta)\cos\theta_{\text{opt}}], \qquad (5)$$

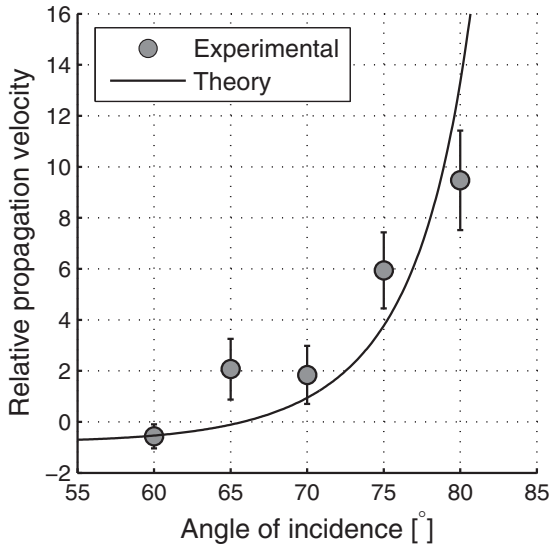

FIG. 11. Relative propagation velocity of the ion-induced pattern as a function of the angle of ion incidence.

where Y_0 is the sputter yield at normal incidence, θ_{opt} is the angle of the maximum sputter yield, and f is a coefficient related to the particular shape of the curve. We obtained the coefficients by fitting the sputter yield angular dependence simulated by SRIM. For 20-keV Ga ions incident on a Ni surface we obtained $Y_0 = 7.2$, $f = 2.71$, and $\theta_{\text{opt}} = 75°$.

Comparison of the experimental data and the theoretical prediction is presented in Fig. 11 and there is a relatively good agreement between the two sets. For 60° the propagation velocity is negative, i.e., the pattern travels towards the ion source. For the higher angles of incidence the propagation velocity changes sign and gradually increases. There are several effects that may contribute to the minor discrepancies between the experimental and theoretical data.

(1) The derivation is based on the precise knowledge of the angular dependence of the sputter yield. Our input is based on the SRIM calculation which is known to be less accurate than some more sophisticated methods [62] and may deviate from the experimental value significantly. Moreover, the sputtering in the present case is likely affected by the ion channeling [53] which may also alter the sputter yield angular dependence.

(2) The theoretical model we use here does not take into account some additional physical effects such as enhanced sputtering at the terrace edges [63] and subsurface ion channeling [64]. These effects were shown to play an important role in the pattern formation on the Pt(111) surface and to strongly affect the ripple pattern regularity and coarsening behavior [54,65] and it is also expectable that these phenomena would influence the pattern propagation. On the other hand, the agreement between the simple theory and our experiments is rather good which indicates that the role of these phenomena is probably not essential in our system.

The theoretical derivation of the propagation velocity (1) is based on the assumption that the surface slopes are small and the surface morphology evolution is in the linear regime. If this condition is not fulfilled the real pattern propagation velocity can deviate substantially from the theoretical prediction [30,45,52]. In our case, the surface angles can be rather substantial; however, the surface is mostly inclined in the direction "across" the ripple pattern while the pattern propagation is linked to the inclination of the surface in the direction parallel to the ion beam. In contrast to the case of PaMRs on amorphizable surfaces, in the present case these two directions are mutually perpendicular and the pattern propagation seems to follow the predictions of the linear theory quite well.

This study is the first one to investigate the propagation of the ion-induced pattern on a metallic surface and, in contrast to all the previous investigations, the ripple pattern orientation is parallel to the ion beam (PeMR). In the previously studied cases of PaMR formation the propagation velocity is perpendicular to the ripple ridges and it is rather straightforward to track the position of a particular crest or valley in the ripple pattern. However, in the case of PeMRs, the observed pattern propagation is parallel to the ripple direction and it is only visible due to the defects in the ripple pattern (i.e., it, obviously, would not be possible to observe or even define the propagation of a perfect, defectless PeMR pattern).

Our preliminary microscopic analysis of the morphology evolution shows that the detailed propagation of the pattern is rather complex. Although the measured propagation velocity expresses the net or mean motion of the surface morphology, different microscopic features in the pattern can propagate at different velocities and sometimes even different directions. This behavior is also related to the apparent increase of the ripple length and pattern "quality" as well as to the ripple coarsening [65] and calls for further investigation.

V. CONCLUSIONS

The in-plane propagation of the ion-induced perpendicular mode ripple pattern was investigated for the first time on a metallic Ni(001) surface. We presented a procedure to evaluate the morphology propagation from a set of SEM images which can also serve as an objective definition of the pattern propagation. The experimental values of the propagation direction and velocity are in a reasonable agreement with the predictions of the classical theory without the obvious need for the inclusion of additional phenomena. In contrast to the previously studied cases of PaMR propagation, the condition of small slopes is naturally well fulfilled for PeMRs due to the specific direction of the ripples with respect to the ion beam. On the other hand, the description of the pattern propagation is more complex since it only relies on defects and imperfections in the ripple pattern. Additional detailed investigation of the pattern defect dynamics is desired in order to fully understand the process of the pattern formation, coarsening, and apparent increase of the ripple pattern regularity with increasing ion fluence.

ACKNOWLEDGMENTS

This work was supported by institutional support from Czech Ministry of Education, Youth and Sports, Grant No. RVO 68407700. M.V. and P.Č. acknowledge support by the Czech Science Foundation under Project No. P204/11/1206.

[1] M. Navez, C. Sella, and D. Chaperot, C. R. Acad. Sci. **254**, 240 (1962).
[2] T. Aste and U. Valbusa, New J. Phys. **7**, 122 (2005).
[3] W. L. Chan and E. Chason, J. Appl. Phys. **101**, 121301 (2007).
[4] B. Ziberi, F. Frost, T. Höche, and B. Rauschenbach, Phys. Rev. B **72**, 235310 (2005).
[5] A. Keller and S. Facsko, Phys. Rev. B **82**, 155444 (2010).
[6] S. Facsko, T. Dekorsy, C. Koerdt, C. Trappe, H. Kurz, A. Vogt, and H. L. Hartnagel, Science **285**, 1551 (1999).
[7] F. Frost, A. Schindler, and F. Bigl, Phys. Rev. Lett. **85**, 4116 (2000).
[8] O. Malis, J. D. Brock, R. L. Headrick, M.-S. Yi, and J. M. Pomeroy, Phys. Rev. B **66**, 035408 (2002).
[9] R. Gago, L. Vázquez, O. Plantevin, J. A. Sánchez-García, M. Varela, M. C. Ballesteros, J. M. Albella, and T. H. Metzger, Phys. Rev. B **73**, 155414 (2006).
[10] R. Gago, L. Vázquez, R. Cuerno, M. Varela, C. Ballesteros, and J. M. Albella, Nanotechnology **13**, 304 (2002).
[11] T. Michely and G. Comsa, Surf. Sci. **256**, 217 (1991).
[12] B. Ziberi, F. Frost, and B. Rauschenbach, J. Vac. Sci. Technol. A **24**, 1344 (2006).
[13] S. A. Mollick, D. Ghose, P. D. Shipman, and R. Mark Bradley, Appl. Phys. Lett. **104**, 043103 (2014).
[14] J.-H. Kim, N.-B. Ha, J.-S. Kim, M. Joe, K.-R. Lee, and R. Cuerno, Nanotechnology **22**, 285301 (2011).
[15] J.-H. Kim, J.-S. Kim, J. Muñoz-García, and R. Cuerno, Phys. Rev. B **87**, 085438 (2013).
[16] F. Buatier de Mongeot and U. Valbusa, J. Phys.: Condens. Matter **21**, 224022 (2009).
[17] Q.-f. Zhan, S. Vandezande, C. Van Haesendonck, and K. Temst, Appl. Phys. Lett. **91**, 122510 (2007).
[18] K. Zhang, M. Uhrmacher, H. Hofsaess, and J. Krauser, J. Appl. Phys. **103**, 083507 (2008).
[19] T. W. H. Oates, A. Keller, S. Facsko, and A. Mücklich, Plasmonics **2**, 47 (2007).
[20] A. Toma, D. Chiappe, C. Boragno, and F. Buatier de Mongeot, Phys. Rev. B **81**, 165436 (2010).
[21] O. Azzaroni, P. L. Schilardi, R. C. Salvarezza, R. Gago, and L. Vazquez, Appl. Phys. Lett. **82**, 457 (2003).
[22] O. Azzaroni, M. Fonticelli, P. L. Schilardi, G. Benítez, I. Caretti, J. M. Albella, R. Gago, L. Vázquez, and R. C. Salvarezza, Nanotechnology **15**, S197 (2004).
[23] R. Cuerno, M. Castro, J. Munoz-Garcia, R. Gago, and L. Vasquez, Nuclear Instruments and Methods in Physics Research B **269**, 894 (2011).
[24] O. Bobes, K. Zhang, and H. Hofsäss, Phys. Rev. B **86**, 235414 (2012).
[25] S. A. Norris, J. Samela, L. Bukonte, M. Backman, F. Djurabekova, K. Nordlund, C. S. Madi, M. P. Brenner, and M. J. Aziz, Nature Communications **2**, 276 (2011).
[26] M. Castro and R. Cuerno, Appl. Surf. Sci. **258**, 4171 (2012).
[27] R. M. Bradley and J. M. E. Harper, J. Vac. Sci. Technol. A **6**, 2390 (1988).
[28] P. Sigmund, Phys. Rev. **184**, 383 (1969).
[29] H. Hofsäss, K. Zhang, H. G. Gehrke, and C. Brüsewitz, Phys. Rev. B **88**, 075426 (2013).
[30] S. Habenicht, K. P. Lieb, J. Koch, and A. D. Wieck, Phys. Rev. B **65**, 115327 (2002).
[31] A. Keller, A. Biermanns, G. Carbone, J. Grenzer, S. Facsko, O. Plantevin, R. Gago, and T. H. Metzger, Appl. Phys. Lett. **94**, 193103 (2009).
[32] T. C. Kim, M. H. Jo, Y. Kim, D. Y. Noh, B. Kahng, and J.-S. Kim, Phys. Rev. B **73**, 125425 (2006).
[33] C. S. Madi, E. Anzenberg, K. F. Ludwig, and M. J. Aziz, Phys. Rev. Lett. **106**, 066101 (2011).
[34] O. El-Atwani, A. Suslova, A. DeMasi, S. Gonderman, J. Fowler, M. El-Atwani, K. Ludwig, and J. Paul Allain, Appl. Phys. Lett. **101**, 263104 (2012).
[35] A. Keller, L. Peverini, J. Grenzer, G. J. Kovacs, A. Mücklich, and S. Facsko, Phys. Rev. B **84**, 035423 (2011).
[36] W. L. Chan and E. Chason, Phys. Rev. B **72**, 165418 (2005).
[37] A.-D. Brown, J. Erlebacher, W.-L. Chan, and E. Chason, Phys. Rev. Lett. **95**, 056101 (2005).
[38] A.-D. Brown and J. Erlebacher, Phys. Rev. B **72**, 075350 (2005).
[39] W. L. Chan, N. Pavenayotin, and E. Chason, Phys. Rev. B **69**, 245413 (2004).
[40] J. Erlebacher, M. J. Aziz, E. Chason, M. B. Sinclair, and J. A. Floro, Phys. Rev. Lett. **82**, 2330 (1999).
[41] S. van Dijken, D. de Bruin, and B. Poelsema, Phys. Rev. Lett. **86**, 4608 (2001).
[42] C. Teichert, C. Ammer, and M. Klaua, Phys. Status Solidi A **146**, 223 (1994).
[43] G. Bracco and D. Cavanna, Phys. Rev. B **76**, 033411 (2007).
[44] B. Poelsema, L. K. Verheij, and G. Comsa, Phys. Rev. Lett. **53**, 2500 (1984).
[45] P. F. A. Alkemade, Phys. Rev. Lett. **96**, 107602 (2006).
[46] Q. Wei, J. Lian, L. A. Boatner, L. M. Wang, and R. C. Ewing, Phys. Rev. B **80**, 085413 (2009).
[47] H. Gnaser, B. Reuscher, and A. Zeuner, Nuclear Instruments and Methods in Physics Research B **285**, 142 (2012).
[48] D. Kramczynski, B. Reuscher, and H. Gnaser, Phys. Rev. B **89**, 205422 (2014).
[49] A. Datta, Y.-R. Wu, and Y. L. Wang, Phys. Rev. B **63**, 125407 (2001).
[50] A. Cuenat, H. B. George, K.-C. Chang, J. M. Blakely, and M. J. Aziz, Adv. Mater. **17**, 2845 (2005).
[51] S. Ichim and M. J. Aziz, J. Vac. Sci. Technol. B **23**, 1068 (2005).
[52] J. Muñoz-García, R. Cuerno, and M. Castro, Phys. Rev. B **78**, 205408 (2008).
[53] T. Skeren, K. Temst, W. Vandervorst, and A. Vantomme, New J. Phys. **15**, 093047 (2013).
[54] H. Hansen, A. Redinger, S. Messlinger, G. Stoian, Y. Rosandi, H. M. Urbassek, U. Linke, and T. Michely, Phys. Rev. B **73**, 235414 (2006).
[55] H. X. Qian, W. Zhou, Y. Q. Fu, B. Ngoi, and G. C. Lim, Appl. Surf. Sci. **240**, 140 (2005).
[56] M. Lenius, R. Kree, and C. A. Volkert, Phys. Rev. B **84**, 035451 (2011).
[57] A. Toma, B. Setina Batic, D. Chiappe, C. Boragno, U. Valbusa, M. Godec, M. Jenko, F. B. de Mongeot, B. S. Batic, and F. Buatier de Mongeot, J. Appl. Phys. **104**, 104313 (2008).
[58] H. Okamoto, J. Phase Equilib. Diffus. **29**, 296 (2008).
[59] J. F. Ziegler, J. P. Biersack, and U. Littmark, *The Stopping and Range of Ions in Solids* (Pergamon, New York, 1985).

[60] J. Biersack and L. Haggmark, Nucl. Instrum. Methods **174**, 257 (1980).
[61] Y. Yamamura and S. Shindo, Radiat. Eff. **80**, 57 (1984).
[62] H. Hofsäss, K. Zhang, and A. Mutzke, Appl. Surf. Sci. **310**, 134 (2014).
[63] A. Redinger, Y. Rosandi, H. M. Urbassek, and T. Michely, Phys. Rev. B **77**, 195436 (2008).
[64] A. Redinger, H. Hansen, U. Linke, Y. Rosandi, H. M. Urbassek, and T. Michely, Phys. Rev. Lett. **96**, 106103 (2006).
[65] H. Hansen, A. Redinger, S. Messlinger, G. Stoian, J. Krug, and T. Michely, Phys. Rev. Lett. **102**, 146103 (2009).